

The downside of downskin: an overhang ratio to digitally evaluate printability of complex architectures by laser powder bed fusion additive manufacturing

Martine McGregor^{a,*}, Sagar Patel^{a,*}, Kevin Zhang^a, Adam Yu^b, Mihaela Vlasea^a, Stewart McLachlin^{a,**}

^aUniversity of Waterloo, Department of Mechanical and Mechatronics Engineering, Waterloo, ON N2L 3G1, Canada

^bUniversity of Waterloo, Department of Systems Design Engineering, Waterloo, ON N2L 3G1, Canada

Abstract

Additive manufacturing (AM) enables new possibilities for the design and manufacturing of complex metal architectures. Incorporating lattice structures into complex part geometries can enhance strength-to-weight and surface area-to-volume ratios for valuable components, particularly in industries such as medicine and aerospace. However, when it comes to metal AM technologies like laser powder bed fusion (LPBF), the design parameters of lattice structures and their interconnections may result in unsupported downskin surfaces, potentially limiting their manufacturability. This study aimed to examine the correlation between downskin surface area and the manufacturability of lattice structures fabricated using LPBF. Image processing algorithms were used to analyze the downskin surface areas of seven unique lattice designs and to devise quantitative metrics (such as downskin surface area, discrete surface count, surface inter-connectivity, overhang ratio, overprint/underprint volumes, etc.) to evaluate LPBF manufacturability. The seven lattice designs were subsequently manufactured using maraging steel via LPBF, and then examined using imaging using X-ray micro-computed tomography (XCT). The geometric accuracy of the lattice designs was compared with XCT scans of the manufactured lattices by employing a voxel-based image comparison technique. The results indicated a strong relationship between downskin surface area, surface interconnectivity, and the manufacturability of a given lattice design. The digital manufacturability evaluation workflow was also applied to a medical device design as an example, further affirming its potential industrial utility for complex geometries.

Keywords: Additive manufacturing, Manufacturability, Powder bed fusion, Lattice structures, Design

*Martine McGregor and Sagar Patel contributed equally to this article

**Corresponding author

Email address: stewart.mclachlin@uwaterloo.ca (Stewart McLachlin)

1. Introduction

Metal additive manufacturing (AM) facilitates new possibilities for complex part geometry design and fabrication [1, 2]. Within metal AM, laser powder bed fusion (LPBF) is commonly used for industrial part production due to superior part resolution [3] and adaptability to different material types [4]. Despite these advantages of LPBF, there remain drawbacks with respect to support structure requirements resulting in surface roughness, post-processing requirements, and material waste. Support structures are typically required on downward facing (downskin) surfaces having angles with respect to the build plate between 0-45 degrees [5]. These downskin surfaces, present in almost all parts designed for metal AM, require support structures for part anchoring and for thermal dissipation to mitigate the risk of excessive material vaporization and distortion due to residual stresses [6]. Unsupported downskin may lead to increased surface roughness, deviations in part geometry, porous defects, reduced mechanical performance, and, in a worst-case scenario, failed prints [7]. Design considerations for downskin surfaces, such as refinement and reduction of downskin part geometry features with respect to part orientation to the build plate, need to be addressed prior to fabrication via LPBF. It can be challenging to completely minimize the occurrence of downskin surfaces from components with complex architectures, one example being interconnected lattice structures with repeating downskin surfaces [5].

Many complex parts in AM incorporate lattice architectures, a form of hierarchical design structures, to improve strength-to-weight and surface area-to-volume ratios through fine-tuning design parameters. Lattice structures vary widely in design and may be surface or strut-based, periodic or stochastic, and/or homogeneous or heterogeneous [5, 8, 9]. Surface-based lattices have a greater surface area-volume ratio than strut-based lattices, making them more suited for applications related to heat exchange, filtration, and biomedical devices wherein osseointegration is important. Whereas strut-based lattices allow for higher strength and stiffness for structural components or load-bearing applications [10]. For high-value components like medical devices, the benefits of utilizing lattice structures within complex part geometries include light-weighting parts through topology optimization, controlling fluid flow, and tailoring biomimetic performance requirements for the human body [5, 11, 12, 13]. Such lattice structures are challenging to manufacture through traditional manufacturing methods due to their geometric complexity [10]. AM offers the adaptability required to produce these valuable metamaterials, independently or integrated as part of larger part geometries. However, lattice structures often have downskin regions that cannot be supported adequately in LPBF due to the interconnectivity of the design features, making removal of support structures nonviable.

The quality of downskin surfaces in LPBF components has been previously examined in literature. It is well established that surfaces between 0-45 degrees to the build plate are prone to poor geometric fidelity and dross, the phenomenon in which partially sintered powder fuses to solid surfaces resulting

in increased surface roughness [14, 15, 16, 17]. Print parameters have been found to affect the manufacturability of downskin surfaces through experiments examining surface angle, scanning speed, laser power, accumulated residual stress, and scanning vector length [18, 19, 20]. Laser scanning strategies can also be controlled through tailored algorithms to improve surface roughness and reduce geometric variation on downskin surfaces [21]. Downskin surfaces have also been shown to increase near-surface porous defects in LPBF parts [22, 23]. In an intensive experimental investigation, Shange et al. [22] reported an inversely proportional relationship between downskin surface angle and near-surface porosity and surface roughness, with a lower downskin angle being associated with greater near-surface porosity and surface roughness. These studies show that there is an overall interplay between process parameters and design that often require significant optimization efforts to ensure manufacturability and geometric fidelity. As such, digital tools that can highlight or predict design features which can present distinct manufacturability challenges based on AM technology-specific constraints would be valuable towards build file optimization and parameter selection; the goal of the present work aims to contribute in addressing this need.

Measuring part tolerance and geometric accuracy is an important aspect of understanding part quality and evaluating manufacturability. Historically, the geometric accuracy of parts has been measured from two-dimensional (2D) cross-sections at features of interest; this technique has been successfully used to complete complex part geometry investigations [24]. Through 2D measurement of part geometry, information concerning over-printing and under-printing of specific regions can be obtained. This is often how dross, or overprinting of downskin surfaces, is measured. Over-printing and under-printing can also be measured volumetrically through analysis of the total part by weight, volume displacement, or X-ray computed tomography (XCT) images [25, 26, 27]. While these techniques provide insight into the overall success of the manufactured part, there is no relationship to where localized over- and/or under-printing has occurred. As such, there is a need for digital tools to better quantify the three-dimensional (3D) geometric fidelity of complex parts produced using AM; efforts in this present work will be dedicated towards the development and deployment of such digital assessment tools for quantifying manufacturability challenges in LPBF of complex design architectures.

Downskin surfaces remain a difficult challenge for AM using LPBF, especially for complex interconnected lattice geometries where downskin support is typically not feasible. The primary goal of this work is to develop digital evaluation tools to identify how and where downskin surfaces are likely to fail within lattice structures produced through LPBF by evaluating the angle, the degree of interconnectivity, and surface area of downskin surfaces within a lattice structure against outcomes from manufactured parts. To achieve this task, digital tools were developed to quantitatively assess manufacturability outcomes for different lattice types relative to downskin characteristics by examining pore defects and 3D geometric part divergence between ideal computer-aided designs (CAD) and

manufactured parts digitally reconstructed via XCT. It was hypothesized that downskin characteristics such as surface area and interconnectivity would correlate to geometric deviations in lattice structures produced through LPBF. The digital evaluation workflow developed was then applied to an example orthopaedic implant design that features lattice structures produced with different materials in order to highlight the adaptability and applicability of the developed tools.

2. Methodology

2.1. Design and evaluation of downskin regions in lattice structures

Seven unique homogeneous periodic lattices were designed to evaluate the effect of downskin surface characteristics on manufacturability: face-centred cubic (FCC), body-centred cubic (BCC), graphical diamond, octet, TPMS gyroid, TPMS Schwarz, and TPMS diamond. Homogeneity (constant) versus heterogeneity (changing) in lattices refers to the thickness of unit cell features such as struts and/or walls [5]. The lattice structures used in this work are homogeneous and have a uniform feature (strut and/or wall) thickness throughout the design space. The seven periodic lattice structures were designed using the nTopology software (nTopology Inc., New York, NY). All lattice geometries were used to fill 20 x 20 x 20 mm cubic design space, with a homogeneous lattice feature thickness of 1 mm, as shown in Figure 1. For the seven periodic lattices, a unit cell size of 10 x 10 x 10 mm was used.

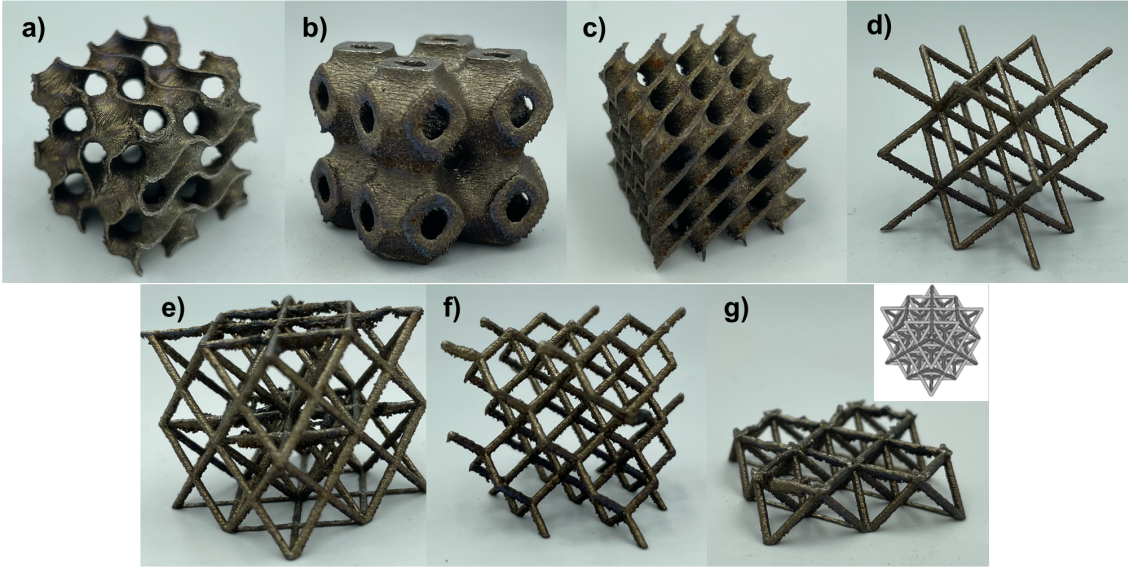


Figure 1: Seven unique homogenous lattice structures were printed using maraging steel through laser powder bed fusion (M290, EOS, Germany): (a) TPMS gyroid, (b) TPMS Schwarz, (c) TPMS diamond, (d) body-centred cubic, (e) face-centred cubic, (f) graphical diamond, and (g) octet (failed).

2.1.1. Evaluation of downskin

Based on the CAD models (in the STL file format) of the lattice structures developed as a reference, the angle between a given downskin surface and the build plate is referred to as the surface angle. Downskin surfaces were then defined as features with a surface angle between 0 and 90 degrees, where 0-degree features are parallel to the build plate and 90-degree surfaces are perpendicular to the build plate, often termed side-skin surfaces. Downskin surfaces with a surface angle below 45 degrees are of particular interest to the AM community due to well-recognized manufacturability challenges. Side-skin surfaces and upskin surfaces, features with a surface angle between 90-180 degrees, are generally considered manufacturable with LPBF technologies and were excluded from analysis in this study.

To understand the impact of surface angle on manufacturability, a custom Python software tool was developed using 3D Slicer (v.4.11) to determine localized surface angles from the CAD models of the different lattice types. 3D Slicer uses the open-source Visualization Toolkit (VTK) for polygonal representation of CAD models from STL files. Two VTK classes, namely `vtkPolyDataNormals` and `vtkMath`, were leveraged in the custom Python script to determine the surface angle of individual polygon cell elements relative to a set normal plane. The normal plane in this case was set to match the LPBF build plate plane to determine the relative surface angle of polygon cells within the lattice structures. The calculated surface angles were then applied to each polygon cell as an associated scalar value.

With this approach, the normal plane, or build plate, has a unit normal of $[0, 0, 1]$ in Cartesian coordinates. The angle between the auto-oriented (outward-facing) unit normal of each polygon cell and the build plate normal was calculated to obtain the surface angle of each triangular mesh element. To better visualize surface angles within the lattice structures, downskin surfaces were discretized into 15-degree surface angle increments and assigned a colour. The 15-degree discretization value was selected based on a balance between discretization of downskin regions for visualization and analysis, prior manufacturability and surface quality challenges reported in literature [28, 29, 30, 31], and observed by the authors through experience. Within each 15-degree increment bin, up to 90 degrees orientation, the total downskin surface area and percentage of total downskin surface per increment bin were calculated. Downskin surfaces in contact with the build plate were excluded from surface area calculations, as these surfaces are supported during the LPBF manufacturing process and therefore do not pose the same challenges as unsupported downskin surfaces. The procedure for quantifying and visualizing downskin surface angles from the lattice structure CAD models is summarized using a flowchart in Figure 2.

2.2. Lattice structure manufacturing and evaluation of manufacturability

The seven homogeneous lattice structures were manufactured with 18Ni-300 maraging steel (Böhler, Germany) using metal AM via LPBF (M290, EOS, Germany). The beam spot diameter of the EOS

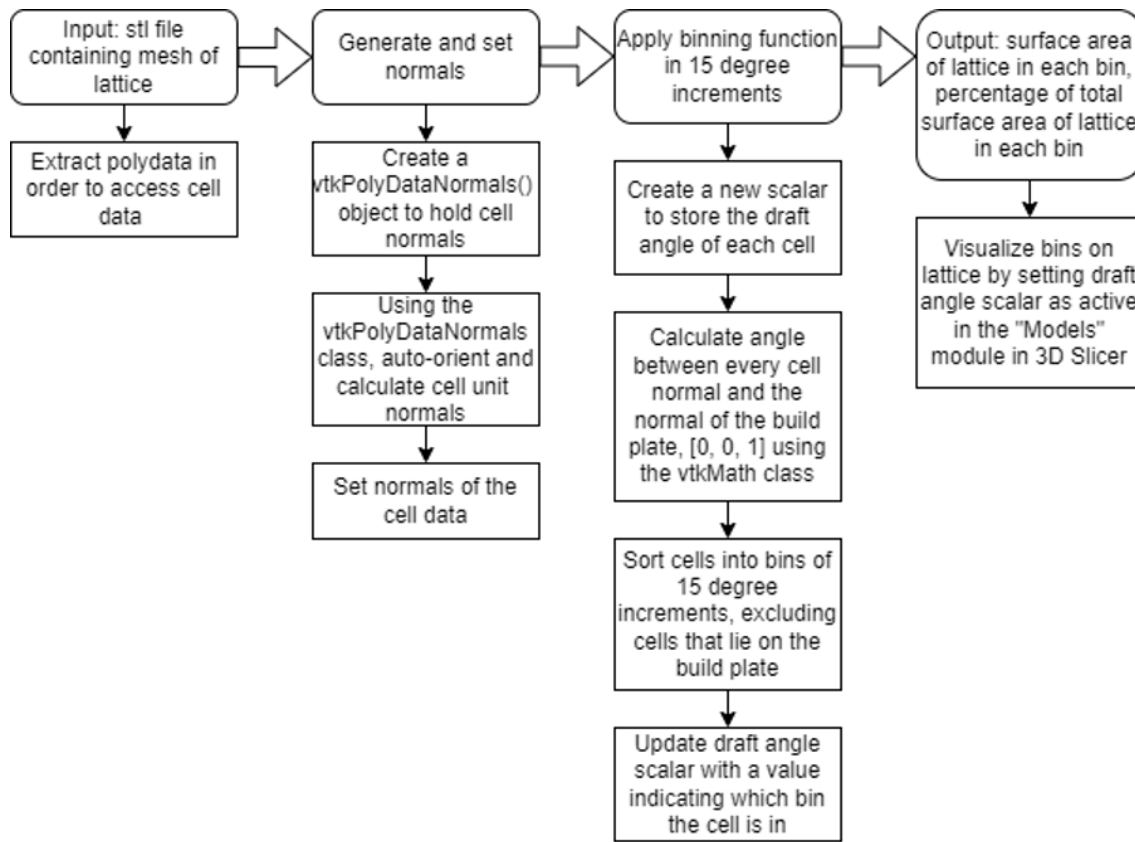


Figure 2: A flowchart to outline the procedure used to quantify surface angles and discretized surfaces into 15-degree increments.

M290 LPBF system used was 90 μm , which was kept constant for the study. The maraging steel powders were gas atomized with a nominal particle size range of 15-43 μm . All the lattice structures were part of the same print. The LPBF print parameters were tailored for complex parts and thereby included different process parameters for the core, contour/border, downskin, and upskin based on a previously developed recipe for maraging steel, and are summarized in Table 1. One contour was used for printing all the lattice structures.

2.2.1. Measurement of part porosity

Following manufacturing, the nine lattice structures were removed from the LPBF build plate using electro-discharge machining (EDM) and were then imaged using an XCT scanner (ZEISS Xradia 520 Versa) for non-destructive evaluation of manufacturing outcomes. A voxel size of 30 μm was used for scanning each lattice structure, captured in a single field of view. An image processing software was used to complete porous defect and geometric fidelity detection and visualization (Dragonfly 3.0, Object Research Systems Inc., Montreal, QC) and MATLAB (version 9.1). Lattice structures were imported

Table 1: Summary of the LPBF print parameters for the nine lattice structures using 18Ni-300 maraging steel on EOS M290 that include: core, contour, downskin and upskin parameters.

Parameter	Core	Contour	Downskin: core & contour	Upskin: core & contour
Power	370 W	321 W	100 W	325 W
Velocity	0.92 m/s	0.74 m/s	1 m/s	1m/s
Hatch distance	0.1 mm	N/A	0.1 mm	0.1 mm
Beam offset	0.05 mm	0.05 mm	N/A	N/A
Hatch rotation	67°	N/A	90°	90°
Overlap with core	N/A	N/A	0.08 mm	0.08 mm
Strategy	Meander	N/A	Meander	Meander
Layer thickness	0.04 mm	N/A	4 layers	2 layers

into the imaging software in the STL format and subjected to a greyscale threshold allowing for segmentation between the solid material and porous defects. Segmentation results were then binarized, and resulting images were used to characterize porous defects based on aspect ratio. Porous defects with an aspect ratio greater than or equal to 0.7 were considered rounded (spherical) defects and porous defects with an aspect ratio lesser than 0.7 were considered irregularly shaped defects. The porous defects within the XCT data volume were then highlighted through manual adjustment of brightness, contrast and opacity. Boolean operators were used to compare the porous defect to solid material ratio to determine overall print porosity.

2.2.2. Measurement of geometric accuracy

A voxel-based comparison method was used to assess the geometric fidelity of the printed parts compared to the original CAD models. The CAD design file for each lattice structure was segmented into a stack of black and white images, with a 30 μm voxel size to match the voxel size resolution from the XCT characterization. This allowed for the data to be represented as arrays of Boolean values, with the presence of material being denoted 1/white and material not present being denoted 0/black. A custom Python script was then developed and employed to compare the CAD and XCT datasets voxel by voxel. Two measures of print inaccuracy were used: over-print and under-print. The over-print percentage was defined by the total number of voxels in which the XCT data returned material present and the CAD geometry returned no material present, normalized by the total number of CAD voxels. Conversely, the under-print percentage was the number of voxels in which the CAD returned material

present but the XCT data did not, again normalized by total CAD volume. These metrics were evaluated both as a total value across the entire part and on a slice-by-slice basis (corresponding roughly to each print layer), in order to produce a more specific understanding of volumetric and local accuracy for the lattice structures. To obtain the layer-by-layer metrics, the overprint and underprint values were normalized by the CAD volume for each layer.

2.2.3. Workflow adaptability to domain shift in end-use product design and material system

In addition to the maraging steel cubic lattice structures, two Ti6Al4V orthopaedic implant designs were manufactured on the same EOS M290 LPBF system using a set of previously optimized processing parameters [32]. The two implants were also evaluated with the digital evaluation workflow to assess the adaptability of the workflow for industry applications. Additionally, the use of another material and a stochastic lattice design for these products helps determine the material and design independence of this workflow for LPBF. Both orthopaedic implants had the same outer geometry; however, internal part latticing was deployed with two different lattice structures, TPMS gyroid and Voronoi. Evaluation of the downskin distribution, measurement of part porosity and geometric accuracy were then performed for the orthopaedic implants to evaluate the adaptability and applicability of the digital evaluation workflow for end-use products.

3. Results

Only 5 of the 7 lattice structures were considered to be successfully manufactured in maraging steel through LPBF. The BCC, graphical diamond, TPMS gyroid, TPMS Schwarz, and TPMS diamond all were successfully printed and were available for further evaluation. The FCC lattice printed in full and was XCT imaged for analysis; however, it had significant part defects and was considered a print failure by visual inspection. The octet lattice structure suffered major print failures and was cancelled during the LPBF printing process (Figure 1); it was hence omitted from the porous defect and geometric accuracy analyses.

3.1. Evaluation of downskin surfaces

The downskin spatial distribution for the seven unique lattice structures was determined using the custom pipeline developed in section 2.1. The downskin angle for the surface of each lattice structure was discretized into 15-degree increments; the results of this discretization are shown in Figure 3. The FCC and octet lattices had the highest percentage of downskin surfaces with a surface angle below 30 degrees with 11.07% and 11.47% respectively, as visualized in Figure 4.

In addition to the area and percentage of downskin in each 15-degree increment, the interconnectivity of downskin regions was analyzed to examine the number of downskin islands with a consistent surface

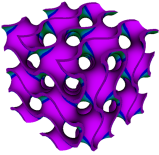
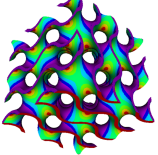
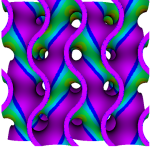







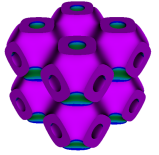
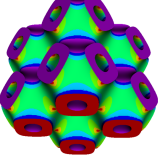
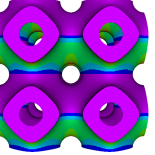







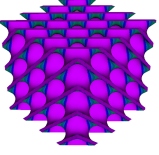
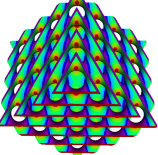
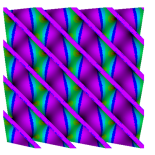







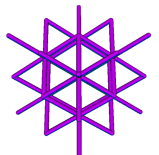
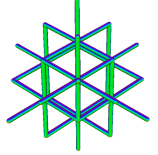
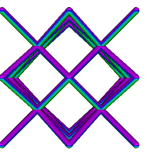







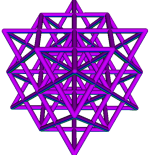
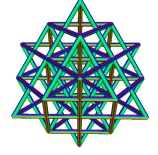
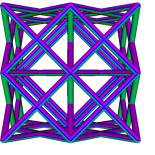







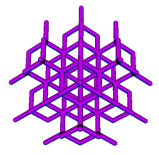
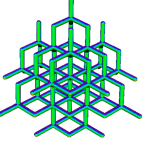
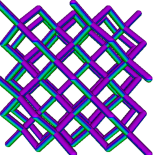







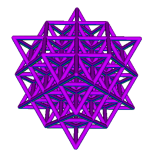
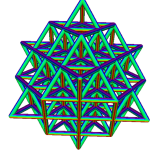
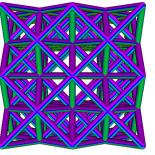







Lattice	Top isometric view	Bottom isometric view	Front view	Color	Downskin angle
TPMS gyroid					0-15°
					15-30°
					30-45°
					45-60°
					60-75°
					75-90°
					90°+
TPMS Schwarz					0-15°
					15-30°
					30-45°
					45-60°
					60-75°
					75-90°
					90°+
TPMS diamond					0-15°
					15-30°
					30-45°
					45-60°
					60-75°
					75-90°
					90°+
Body centered cubic					0-15°
					15-30°
					30-45°
					45-60°
					60-75°
					75-90°
					90°+
Face centered cubic					0-15°
					15-30°
					30-45°
					45-60°
					60-75°
					75-90°
					90°+
Graphical diamond					0-15°
					15-30°
					30-45°
					45-60°
					60-75°
					75-90°
					90°+
Octet					0-15°
					15-30°
					30-45°
					45-60°
					60-75°
					75-90°
					90°+

Figure 3: Seven unique homogeneous lattice structures were evaluated for downskin regions ranging from 0 to 90 degrees of downskin in 15-degree increments: TPMS gyroid, TPMS Schwarz, TPMS diamond, body-centred cubic, face-centred cubic (partially failed), graphical diamond, and octet (failed).

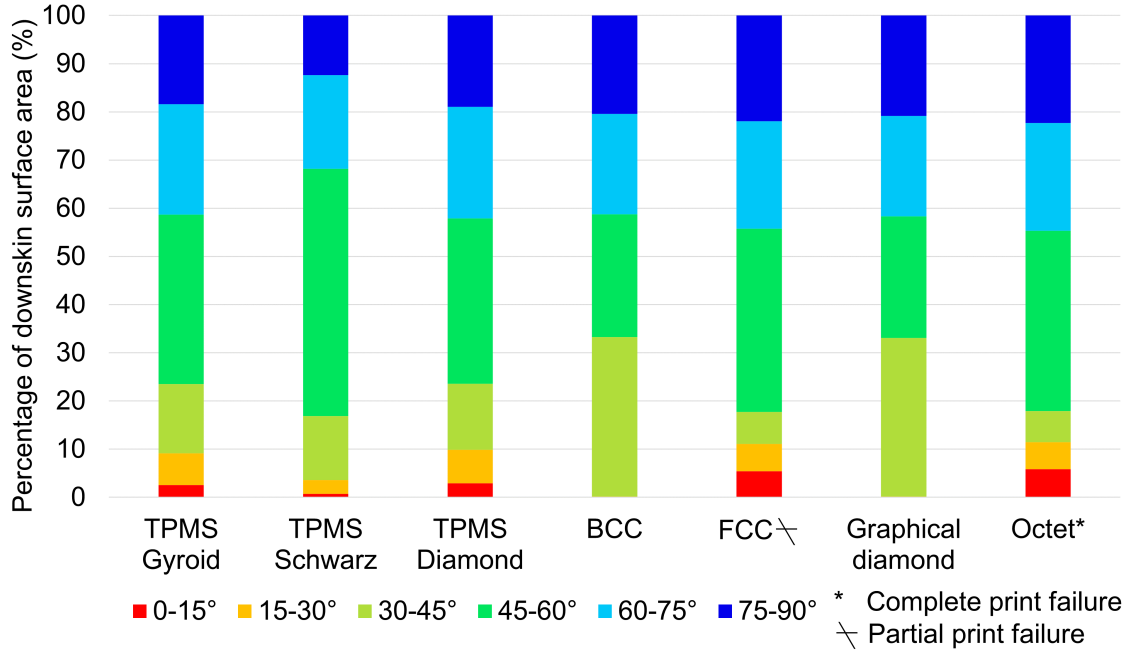


Figure 4: Downskin distribution as determined using the custom 3D Slicer algorithm and discretized into 15° increments. Amongst the seven homogeneous lattice structures, FCC and octet lattices have the highest percentage of downskin surfaces with an angle <30° at 11.07% and 11.47% respectively.

angle between 0-15 degrees. From this island calculation step, an overhang ratio was defined in Equation 1 that is given by the total 0-15 degrees downskin surface area divided by the number of 0-15 degrees downskin islands.

$$\text{Overhang ratio} = \frac{\text{Surface area of 0-15 degrees overhang islands}}{\text{Number of 0-15 degrees overhang islands}} \quad (1)$$

The interconnectivity of downskin surfaces with a downskin angle between 0-15 degrees was quantified by the overhang ratio method. The overhang ratio was calculated for all the lattice structures in Table 2. It was found that the lattice structures that printed successfully had an overhang ratio of less than (<) 1, whereas lattice structures that failed to print had an overhang ratio greater than (>) 1, an illustration of the interconnectivity of such 0-15-degree downskin surfaces is illustrated for select lattices as shown in Figure 5.

3.2. Evaluation of manufacturability

Overall, the lattice structures evaluated in this study had very little porosity, with the most porous being the TPMS Schwarz (99.90% dense) and the least porous being the TPMS gyroid and the graphical diamond (99.99% dense), demonstrating that the process parameters for printing were appropriate in creating consistent thin features (struts and thin walls). Defect types, irregular or round, were

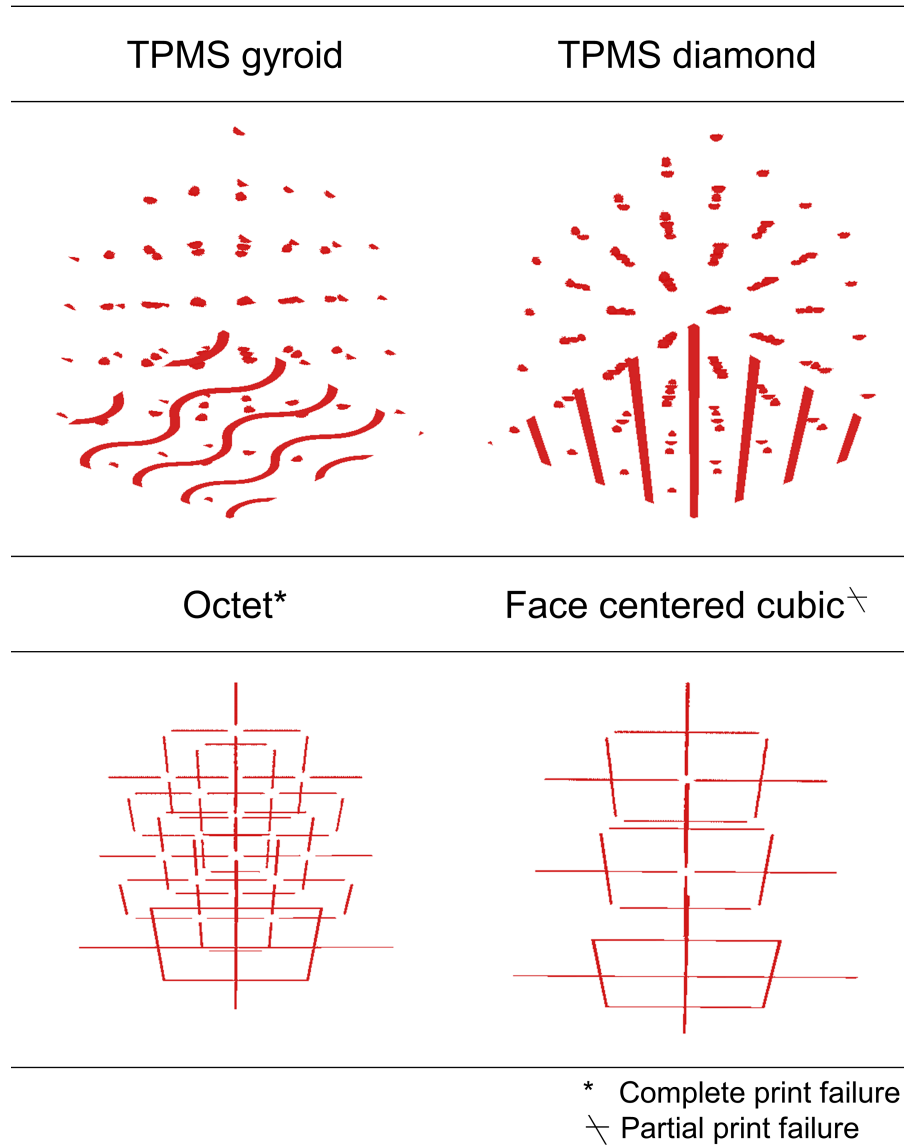


Figure 5: Discrete downskin regions with an angle of 15 degrees or less to the build plate were isolated with the aim of better understanding the effect of downskin area and interconnectivity of downskin islands on printability challenges. The downskin islands for the TPMS gyroid (top left), TPMS diamond (top right), octet (bottom left) and face-centred cubic (bottom right) lattice structures are visualized above.

Table 2: Calculated values of the surface area of overhang features, number of discrete overhang features, and overhang ratio for the seven homogeneous periodic lattice structures manufactured using LPBF in this study.

Lattice structure	Surface area of overhang features <15°(mm ²)	Number of discrete overhang features <15°	Overhang ratio (mm ² /no. of features)
TPMS gyroid	62.4	80	0.78
TPMS Schwarz	12.1	48	0.25
TPMS diamond	89.5	128	0.70
BCC	0.54	9	0.06
FCC	82.1	65	1.26
Graphical diamond	0.78	13	0.06
Octet	119.0	9	13.22

also visualized. Few defects were visible within the lattice structures, which may be attributed to the coarse resolution of the XCT. As an illustration, the XCT of the TPMS Schwarz lattice can be seen in Figure 6, where irregular porous defects are in blue and round porous defects are in red. Those porous defects that were present, were clustered along the downskin regions of the parts as previously shown by Shange et al. [22]. The qualitative pore visualization is further confirmation that porous defects are closely related to the interplay between process parameters and the design in the downskin region.

The seven lattice structures that were printed to completion were analyzed based on the over-print and under-print metrics described in section 2.2.2. The TPMS lattice structures printed more accurately to the design CAD than the strut-based lattices did, for both over-print volume and under-print volume, as captured in Table 3. In order to illustrate the relationship between surface angle and geometric print fidelity, the slice-by-slice overprint and underprint data were aligned and compared. The TPMS gyroid and the FCC were used as examples from the surface-based and strut-based categories, respectively. Figure 7 shows that a small downskin angle aligns with a peak in over-printing, while up-skin surfaces align with a peak in under-printing. These phenomena are more pronounced for the FCC lattice structure where large unsupported overhangs are present. The FCC lattice analysis shows two large spikes in layer overprint, which correspond to the areas of zero-degree downskin angle. Significant dross formation is visible on the superimposed XCT/CAD data. Layer-by-layer comparisons of the XCT and CAD data for the remaining four successfully printed homogeneous periodic lattice structures are provided in Supplementary Information Figure 1.

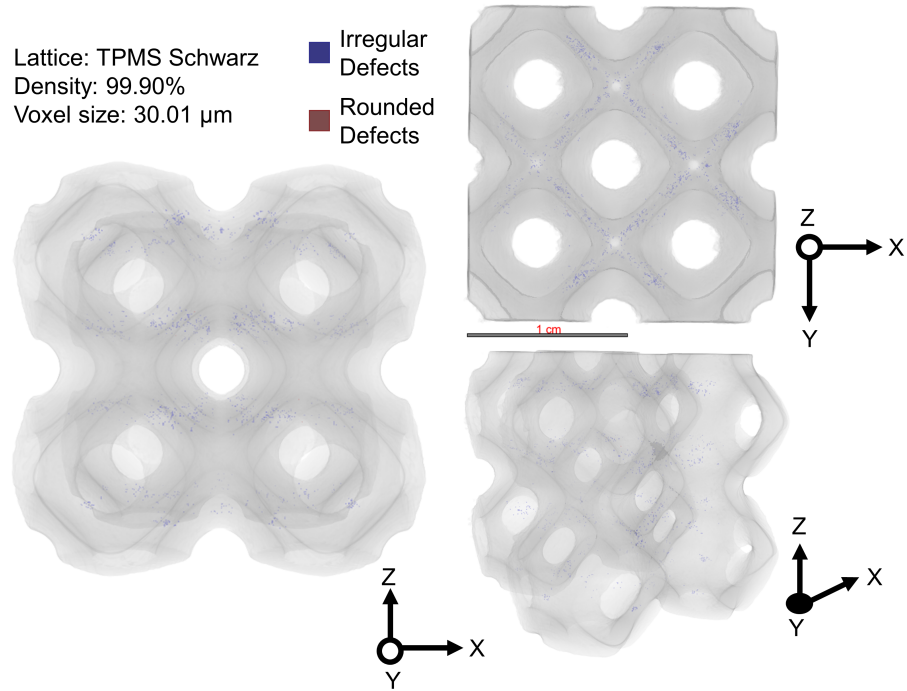


Figure 6: A X-ray computed tomography image of a maraging steel TPMS Schwarz lattice structure produced with laser powder bed fusion is visualized in frontal (left), side (top right) and isometric (bottom right) views. Irregular (blue) and round (red) porous defects are coloured to depict the prevalence and location.

Table 3: Total volumetric over-print and under-print evaluation using the CAD and XCT data of the eight successfully manufactured structures.

Lattice structure	Percent volume overprint (%)	Percent volume underprint (%)
TPMS gyroid	5.3	21.6
TPMS Schwarz	2.7	11.3
TPMS diamond	5.2	21.7
BCC	7.5	32.4
FCC	16.0	31.3
Graphical diamond	8.9	32.6
Interbody cage: gyroid	21.3	8.5
Interbody cage: Voronoi	30.2	13.0

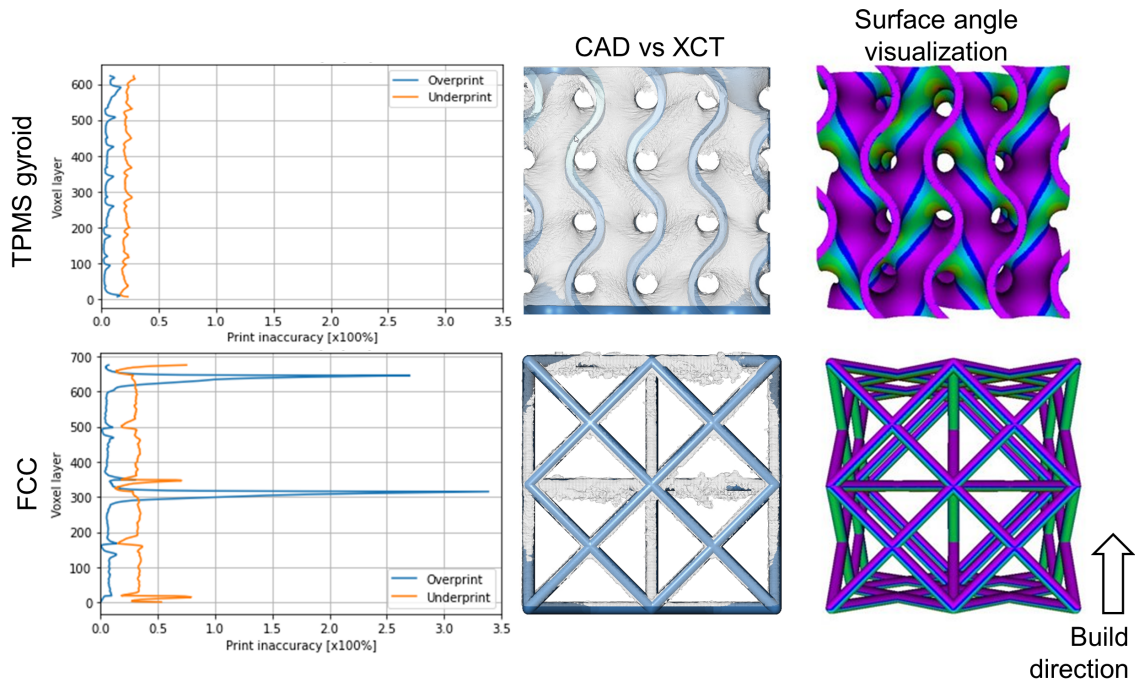


Figure 7: Surface-based lattices, such as the triply periodic minimal surface (TPMS) gyroid (top), were found to be more printable than strut-based lattices, such as the FCC (bottom). The TPMS gyroid had 5.3% and 21.6% volumetric over- and under-print respectively, while the FCC had 16.0% and 31.3% (left, plots). When aligning quantitative values for overprint and underprint to X-ray computed tomography (XCT) (middle, visualizations, where blue is XCT and white is CAD) and surface angle (right, visualization), a clear association between downskin surfaces and poor print quality becomes apparent.

3.2.1. Example applicability to an industrial application

The two orthopaedic implant designs had a greater percentage of total downskin surface area under 15 degrees with respect to the build plate orientation when compared to most of the cubic lattice structures previously examined (as seen in Figure 8 (left)); however, they were considered manufacturable due to the large distribution of small downskin regions throughout the part, as indicated by a overhang ratio of less than one (<1) and illustrated in Figure 8 (right). Layer-by-layer comparisons of the XCT and CAD data for the two implant structures are provided in Supplementary Information Figure 2, which shows the successful manufacturing of the two implant designs using AM due to an overhang ratio < 1 .

4. Discussion

Lattice type was the first factor taken into consideration when examining the overall manufacturability of complex lattice architectures with respect to the downskin surface areas. Comparing the strut-based lattices, the FCC and octet strut-based lattices have long struts whose central axis runs parallel to the build plate, unlike BCC and graphical diamond lattices, where strut elements are at a

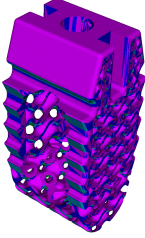
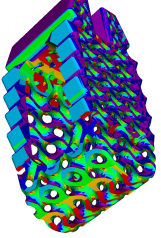
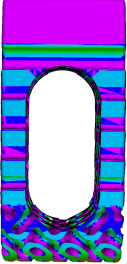

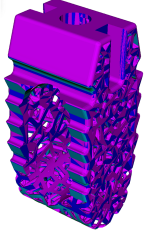
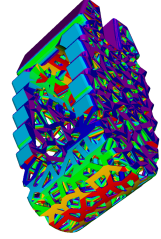
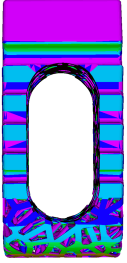

Design	Top isometric view	Bottom isometric view	Front view	Discrete surfaces <15°	Surface area <15° (mm ²)	Overhang ratio
Interbody cage – gyroid					105.52	<1
Interbody cage - Voronoi					134.24	<1

Figure 8: (Left) Downskin distribution within the complete orthopaedic implant parts was determined using a custom algorithm and discretized into 15-degree increments. Distribution for the TPMS gyroid and Voronoi cubic designs were included for comparison. (Right) The two light-weighted orthopaedic implants were evaluated for downskin regions ranging from 0 to 90 degrees of downskin in 15-degree increments. Discrete downskin regions with an angle of 15 degrees or less to the build plate were isolated to determine an overhang ratio with the aim of better understanding the effect of downskin on manufacturability challenges.

minimum of 45 degrees to the build plate. This leads to a significant amount of challenging downskin surfaces with a surface angle below 15 degrees in the FCC and octet as evident in Figure 5. Surface features that were parallel to and touching the build plate were excluded from the downskin analysis. Excluding the failed FCC and octet lattices, the TPMS diamond and TPMS gyroid have the highest percentage of downskin between 0 and 30 degrees, as shown in Figure 4. However, TPMS lattices (gyroid, diamond, and Schwarz) also have a significant amount of surface area touching the build plate and are all successfully manufactured using LPBF. This could be associated with the improved heat transfer to the solid metal on the LPBF build plate, when compared to printing on a powder bed which is known to have significantly lower thermal conductivity [33] and density [34].

The distribution of overhang features (unsupported downskin surfaces between 0-15 degrees) was also found to have an effect on the manufacturability of complex architectures. The TPMS gyroid lattice structure had 80 discrete features with a consistent surface angle between 0-15 degrees. Similarly, the TPMS diamond has 128 discrete features with a consistent surface angle between 0-15 degrees. However, the overall surface area for these overhang features was relatively small for these lattice types,

leading to a downskin ratio of 0.78 and 0.70 for the TPMS gyroid and TPMS diamond, respectively. The regions of interest in both lattices exhibit saddle-like geometry which has been shown to be suitable for additive manufacturing [35, 36]. The FCC and octet lattices had fewer but larger connected overhang features between 0-15 degrees leading to a downskin ratio of 13.22 and 1.26, respectively. These regions are not saddle-shaped and are located at the underside of struts, which are perfectly parallel to the build plate (0 degrees downskin angle). A large surface area of unsupported overhang features (0-15 degrees) likely contributes to manufacturability challenges for the FCC and octet lattice structures. It is known that stress accumulation occurs as the surface area of a given discrete region increases and thereby increasing the risk of defects [21]. Therefore, the overhang ratio term proposed in this work may be a useful tool in digitally evaluating part manufacturability using AM as it provides a more comprehensive characterization of downskin surfaces.

To better understand the effect of the overhang ratio on the manufacturability of the various lattice structures, Figure 9 provides a comparison of the average overprint and underprint between the CAD and XCT for all the eight successfully manufactured structures, with standard deviations provided for the slice-by-slice comparisons. As expected, amongst the homogeneous periodic lattice structures that printed, the FCC lattice structure (considered to be a partial failure) exhibits the highest average as well as standard deviation in terms of overprinting when the CAD and XCT data are compared. The high standard deviation in particular is related to the two large overhang (0-15 degrees) features of the lattice structure that are shown to have volumetric overprint of $\sim 330\%$ in the printed part as shown in Figure 7. These overhang features within the FCC lattice structure are effectively parallel to the LPBF build plate which would typically require support structures for improving thermal conductivity [37], reducing part deformation [38], and preventing cross formation [19] in LPBF.

Table 4: Porosity fraction (of the CAD designs) and mass ratio (actual mass/CAD mass) for the six successfully manufactured homogeneous periodic lattice structures.

Lattice structure	Porosity fraction of CAD (%)	Ratio of actual mass (from XCT) over CAD mass (%)
TPMS gyroid	80.66	83.76
TPMS Schwarz	65.7	91.35
TPMS diamond	76.82	83.51
BCC	94.89	75.23
FCC	90.81	84.62
Graphical diamond	94.88	76.27

A relatively large volumetric underprint is observed in all of the homogeneous periodic lattice

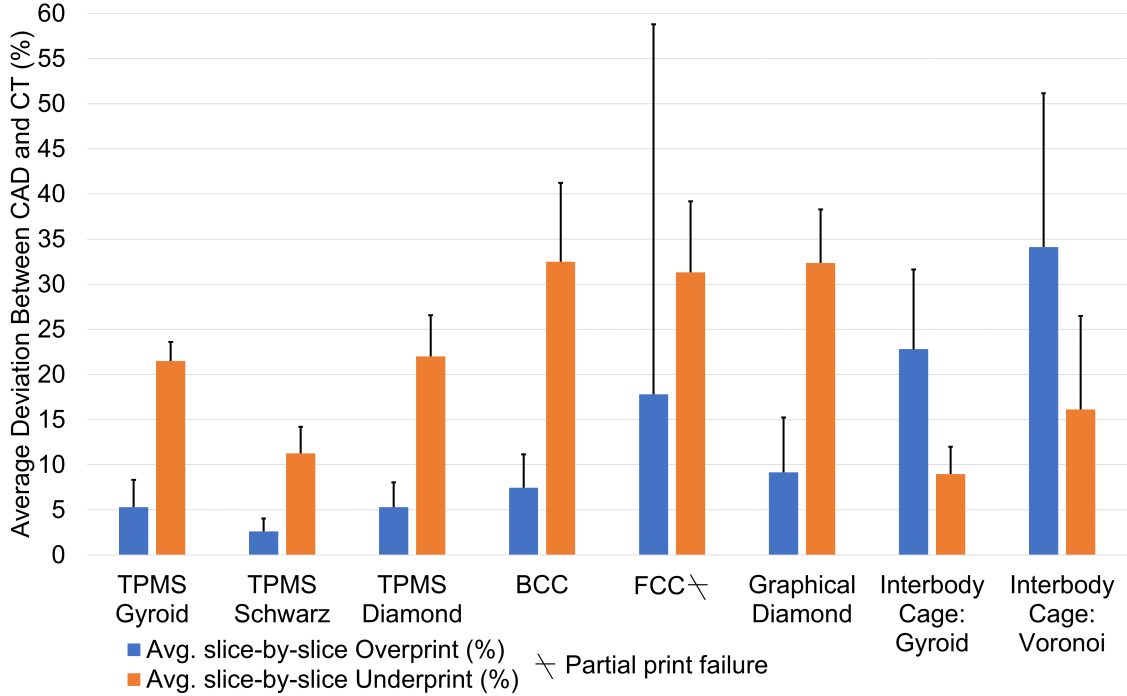


Figure 9: Average and standard deviations for volumetric over-print and under-print from slice-by-slice comparisons of the CAD and XCT data of the eight successfully manufactured structures.

structures (Table 3 and Figure 9). For the TPMS lattices, the total volumetric underprint is between 11.3-21.7% as shown in Table 3. For the strut-based lattices, the total volumetric underprint is significantly higher when compared to the TPMS lattices (31.3-32.6%, as shown in Table 3). Overall, all lattices did underprint when compared to the designed CAD (75-91%), as shown by the ratio of the actual mass (from XCT data) to the CAD mass in Table 4. The underprinting observed in all lattices can be partly explained by shrinkage caused by the melting of porous powder followed by rapid solidification in LPBF, and has been reported for TPMS lattices in literature [39, 40]. Additionally, laser power [41], scanning speed [41], layer thickness [41], and build plate location of a given part [42] are other factors that could have effects on shrinkage [41].

Layer-by-layer specimen geometry is known to have significant effects on shrinkage as well [43] since it would directly influence the boundary conditions for the following layer, in the sense of whether or not a given feature in the current layer is supported by solidified metal or the powder bed, both of which have significantly different thermal conductivity values [33]. Porosity fraction for the surface-based (TPMS) and strut-based lattice designs in Table 4 can help understand the expected differences in layer-by-layer geometry. In Table 4, the porosity fraction of a given lattice structure design is calculated as $1 - Volume\ fraction$, wherein volume fraction denotes the volume of the lattice structure CAD divided by the volume of the solid cube model ($20 \times 20 \times 20 \text{ mm}^3$). The porosity fractions of all strut-based

lattice designs are $>90\%$ whereas the porosity fractions of all surface-based (TPMS) lattice designs are between 65-80%. The higher porosity fraction in strut-based lattice designs would mean that there is a higher probability that for a given feature in a given layer, the underlying boundary conditions are more likely to be driven by the poor thermal conductivity powder bed for strut-based lattices, when compared to the surface-based lattices. A powder bed driven boundary condition would mean that for strut-based lattices, the melted portions of a given layer would also be on a relatively low-density powder bed, which would lead to a higher volumetric overprint due to dross formation, as well as underprint due to shrinkage and potential distortion of the overhanging features due to poor thermal conductivity of the powder bed [44]. A higher porosity fraction in strut-based lattice designs, as shown in Table 4 is thereby expected to cause the high volumetric underprint and overprint observed in Figure 9 and Table 3, as also reported by Taib et al. [45]. It must be noted that imperfect alignment of the XCT and CAD datasets during analysis could also lead to some of the underprint and overprint values observed in this study.

An additional two orthopaedic implant designs were evaluated to assess the adaptability of the proposed digital workflow for biomedical applications. Two orthopaedic implant designs were light-weighted with either a periodic TPMS lattice structure (gyroid) or a stochastic Voronoi lattice structure. Both the implant designs have an overhang ratio <1 as shown in Figure 8, and both implants did print successfully. Both implants, however, have a higher volumetric overprint when compared to the successfully printed homogeneous lattice structures (except the FCC, which is considered a partial failure, and has the highest volumetric overprint when the standard deviation is considered, as shown in Figure 9) and Supplementary Information Figure 1. The higher overprint for the implant designs is partly related to the use of support structures at the bottom of the implants during prints, which could not be completely removed during the XCT versus CAD analysis. Additionally, an exact alignment of the highly complex implant designs to the XCT dataset is challenging, which could add to inaccuracies in the reported underprint and overprint values for the two designs. Regardless, the trend of the surface-based (TPMS) lattice design is seen to again outperform a strut-based stochastic Voronoi lattice design, in terms of both volumetric underprinting and overprinting.

The current study thereby presents a novel approach to quantify and validate the relationship between downskin surfaces for a given design and manufacturability of the designs manufactured using LPBF. The downskin surface of multiple lattice types was evaluated using an image processing workflow to develop the overhang ratio term as a means to quantify the printability of a given design. Designs with overhang ratios lesser than one are expected to print successfully with high dimensional fidelity between the CAD and printed coupons. Such an approach would help reduce the transition from design ideas to successful prints in LPBF.

5. Conclusions

The current study presents a novel digital evaluation workflow to determine the surface area and nature of downskin regions on complex interconnected parts as well as a new approach for evaluating geometric fidelity as a function of volumetric over- and under-printing. Seven unique lattice structures were generated for downskin evaluation. Six lattice structures were successfully manufactured and evaluated for the relationship between down-skin and geometric fidelity. A higher percentage of overhang surface area with a surface angle of 15 degrees or less and an overhang ratio greater than one were indicators of poor geometric fidelity in the final parts. By characterizing the complex 3D interconnectivity of lattice structures, the robustness of the digital workflow was exhibited. The workflow was successfully applied to orthopaedic designs to validate the adaptability to complex part geometries outside of individual unit cells. These tools aim to assist in the evaluation of designs for manufacturability as well as serve to evaluate the success of final 3D printed parts using LPBF.

6. Acknowledgements

Martine McGregor is supported by the Natural Sciences and Engineering Research Council of Canada (NSERC) Canada Graduate Scholarship - Doctoral Award. Sagar Patel, Kevin Zhang, and Mihaela Vlasea appreciate the funding support received from Federal Economic Development Agency for Southern Ontario (FedDev Ontario grant number 814654). Additionally, Sagar Patel, Kevin Zhang, and Mihaela Vlasea would like to acknowledge the help of Jerry Ratthapakdee and Henry Ma with the deployment and characterization of the laser powder bed fusion builds. The authors would like to thank nTopology, Inc. for supporting us with a license to their software for the lattice visualizations.

References

- [1] J. Gardan, Smart materials in additive manufacturing: state of the art and trends, *Virtual and Physical Prototyping* 14 (1) (2019) 1–18.
- [2] D. W. Rosen, Research supporting principles for design for additive manufacturing: This paper provides a comprehensive review on current design principles and strategies for am, *Virtual and physical prototyping* 9 (4) (2014) 225–232.
- [3] W. J. Sames, F. List, S. Pannala, R. R. Dehoff, S. S. Babu, The metallurgy and processing science of metal additive manufacturing, *International materials reviews* 61 (5) (2016) 315–360.
- [4] S. L. Sing, J. An, W. Y. Yeong, F. E. Wiria, Laser and electron-beam powder-bed additive manufacturing of metallic implants: A review on processes, materials and designs, *Journal of Orthopaedic Research* 34 (3) (2016) 369–385.

- [5] M. McGregor, S. Patel, S. McLachlin, M. Vlasea, Architectural bone parameters and the relationship to titanium lattice design for powder bed fusion additive manufacturing, *Additive Manufacturing* 47 (2021) 102273.
- [6] P. Mercelis, J.-P. Kruth, Residual stresses in selective laser sintering and selective laser melting, *Rapid prototyping journal* (2006).
- [7] A. Ashby, G. Guss, R. K. Ganeriwala, A. A. Martin, P. J. DePond, D. J. Deane, M. J. Matthews, C. L. Druzgalski, Thermal history and high-speed optical imaging of overhang structures during laser powder bed fusion: A computational and experimental analysis, *Additive Manufacturing* 53 (2022) 102669.
- [8] H. N. Wadley, Multifunctional periodic cellular metals, *Philosophical Transactions of the Royal Society A: Mathematical, Physical and Engineering Sciences* 364 (1838) (2006) 31–68.
- [9] G. Dong, Y. Tang, Y. F. Zhao, A survey of modeling of lattice structures fabricated by additive manufacturing, *Journal of Mechanical Design* 139 (10) (2017) 100906.
- [10] A. du Plessis, S. M. J. Razavi, M. Benedetti, S. Murchio, M. Leary, M. Watson, D. Bhate, F. Berto, Properties and applications of additively manufactured metallic cellular materials: A review, *Progress in Materials Science* (2021) 100918.
- [11] E. Boccini, R. Furferi, L. Governi, E. Meli, A. Ridolfi, A. Rindi, Y. Volpe, Toward the integration of lattice structure-based topology optimization and additive manufacturing for the design of turbomachinery components, *Advances in Mechanical Engineering* 11 (8) (2019) 1687814019859789.
- [12] C. Zhang, S. Wang, J. Li, Y. Zhu, T. Peng, H. Yang, Additive manufacturing of products with functional fluid channels: A review, *Additive Manufacturing* 36 (2020) 101490.
- [13] S. Patel, M. McGregor, S. McLachlin, M. Vlasea, Digital manufacturing challenge: Rapid deployment of patient-specific prosthesis in emergency medicine enabled by additive manufacturing, *Manufacturing Engineering* 116 (12) (2021) 9–11.
- [14] F. Calignano, Design optimization of supports for overhanging structures in aluminum and titanium alloys by selective laser melting, *Materials & Design* 64 (2014) 203–213.
- [15] A. Triantaphyllou, C. L. Giusca, G. D. Macaulay, F. Roerig, M. Hoebel, R. K. Leach, B. Tomita, K. A. Milne, Surface texture measurement for additive manufacturing, *Surface topography: metrology and properties* 3 (2) (2015) 024002.

- [16] J. C. Fox, S. P. Moylan, B. M. Lane, Effect of process parameters on the surface roughness of overhanging structures in laser powder bed fusion additive manufacturing, *Procedia Cirp* 45 (2016) 131–134.
- [17] H. Chen, D. Gu, J. Xiong, M. Xia, Improving additive manufacturing processability of hard-to-process overhanging structure by selective laser melting, *Journal of Materials Processing Technology* 250 (2017) 99–108.
- [18] D. Wang, Y. Yang, Z. Yi, X. Su, Research on the fabricating quality optimization of the overhanging surface in slm process, *The International Journal of Advanced Manufacturing Technology* 65 (9) (2013) 1471–1484.
- [19] A. Charles, A. Elkaseer, U. Paggi, L. Thijs, V. Hagenmeyer, S. Scholz, Down-facing surfaces in laser powder bed fusion of ti6al4v: Effect of dross formation on dimensional accuracy and surface texture, *Additive Manufacturing* 46 (2021) 102148.
- [20] V. Viale, J. Stavridis, A. Salmi, F. Bondioli, A. Saboori, Optimisation of downskin parameters to produce metallic parts via laser powder bed fusion process: an overview, *The International Journal of Advanced Manufacturing Technology* (2022) 1–24.
- [21] H. Yeung, B. Lane, J. Fox, Part geometry and conduction-based laser power control for powder bed fusion additive manufacturing, *Additive manufacturing* 30 (2019) 100844.
- [22] M. Shange, I. Yadroitsava, A. du Plessis, I. Yadroitsev, Roughness and near-surface porosity of unsupported overhangs produced by high-speed laser powder bed fusion, *3D Printing and Additive Manufacturing* (2021).
- [23] F. Cabanettes, A. Joubert, G. Chardon, V. Dumas, J. Rech, C. Grosjean, Z. Dimkovski, Topography of as built surfaces generated in metal additive manufacturing: A multi scale analysis from form to roughness, *Precision Engineering* 52 (2018) 249–265.
- [24] G. Meyer, J. Musekamp, F. Göbel, F. Gardian, C. Mittelstedt, Manufacturability investigation of inclined als10mg lattice struts by means of selective laser melting, *Manufacturing Letters* 31 (2022) 101–105.
- [25] C. G. Klingaa, M. K. Bjerre, S. Baier, L. De Chiffre, S. Mohanty, J. H. Hattel, Roughness investigation of slm manufactured conformal cooling channels using x-ray computed tomography, in: *Proceedings of the 9th Conference on Industrial Computed Tomography (ICT 2019)*, Padova, Italy, 2019, pp. 13–15.

- [26] T. Puttonen, Evaluation of metal lattice structures with x-ray micro-computed tomography: Dimensional accuracy and manufacturability, in: ASME International Mechanical Engineering Congress and Exposition, Vol. 84539, American Society of Mechanical Engineers, 2020, p. V006T06A015.
- [27] N. Tanlak, D. F. De Lange, W. Van Paepegem, Numerical prediction of the printable density range of lattice structures for additive manufacturing, *Materials & Design* 133 (2017) 549–558.
- [28] K. Alrbaey, D. Wimpenny, R. Tosi, W. Manning, A. Moroz, On optimization of surface roughness of selective laser melted stainless steel parts: a statistical study, *Journal of Materials Engineering and Performance* 23 (2014) 2139–2148.
- [29] E. E. Covarrubias, M. Eshraghi, Effect of build angle on surface properties of nickel superalloys processed by selective laser melting, *Jom* 70 (2018) 336–342.
- [30] J. Zhang, A. Chaudhari, H. Wang, Surface quality and material removal in magnetic abrasive finishing of selective laser melted 316l stainless steel, *Journal of manufacturing processes* 45 (2019) 710–719.
- [31] G. Tarakçı, H. M. Khan, M. S. Yılmaz, G. Özer, Effect of building orientations and heat treatments on alsil0mg alloy fabricated by selective laser melting: microstructure evolution, mechanical properties, fracture mechanism and corrosion behavior, *Rapid Prototyping Journal* 28 (8) (2022) 1609–1621.
- [32] S. Patel, A. Rogalsky, M. Vlasea, Towards understanding side-skin surface characteristics in laser powder bed fusion, *Journal of Materials Research* 35 (15) (2020) 2055–2064.
- [33] L. C. Wei, L. E. Ehrlich, M. J. Powell-Palm, C. Montgomery, J. Beuth, J. A. Malen, Thermal conductivity of metal powders for powder bed additive manufacturing, *Additive Manufacturing* 21 (2018) 201–208.
- [34] T. M. Wischeropp, C. Emmelmann, M. Brandt, A. Pateras, Measurement of actual powder layer height and packing density in a single layer in selective laser melting, *Additive Manufacturing* 28 (2019) 176–183.
- [35] A. Jones, M. Leary, S. Bateman, M. Easton, Effect of surface geometry on laser powder bed fusion defects, *Journal of Materials Processing Technology* 296 (2021) 117179.
- [36] G. A. Adam, D. Zimmer, Design for additive manufacturing—element transitions and aggregated structures, *CIRP Journal of Manufacturing Science and Technology* 7 (1) (2014) 20–28.

- [37] Z.-D. Zhang, O. Ibhádode, U. Ali, C. F. Dibia, P. Rahnama, A. Bonakdar, E. Toyserkani, Topology optimization parallel-computing framework based on the inherent strain method for support structure design in laser powder-bed fusion additive manufacturing, *International Journal of Mechanics and Materials in Design* 16 (2020) 897–923.
- [38] A. Khobzi, F. F. Mehr, S. Cockcroft, D. Maijer, S. L. Sing, W. Y. Yeong, The role of block-type support structure design on the thermal field and deformation in components fabricated by laser powder bed fusion, *Additive Manufacturing* 51 (2022) 102644.
- [39] A. Mulhi, S. Dehgahi, P. Waghmare, A. Qureshi, Dimensional assessment of uniformly periodic porosity primitive tpms lattices using additive manufacturing laser powder bed fusion technique, *The International Journal of Advanced Manufacturing Technology* (2022) 1–22.
- [40] I. Echeta, X. Feng, B. Dutton, R. Leach, S. Piano, Review of defects in lattice structures manufactured by powder bed fusion, *The International Journal of Advanced Manufacturing Technology* 106 (2020) 2649–2668.
- [41] Y. Liu, Y. Yang, D. Wang, Investigation into the shrinkage in z-direction of components manufactured by selective laser melting (slm), *The International Journal of Advanced Manufacturing Technology* 90 (2017) 2913–2923.
- [42] J. K. Veetil, M. Khorasani, A. Ghasemi, B. Rolfe, I. Vrooijink, K. Van Beurden, S. Moes, I. Gibson, Build position-based dimensional deviations of laser powder-bed fusion of stainless steel 316L, *Precision engineering* 67 (2021) 58–68.
- [43] V. Chahal, R. M. Taylor, A review of geometric sensitivities in laser metal 3d printing, *Virtual and Physical Prototyping* 15 (2) (2020) 227–241.
- [44] L. Zhang, Y. Li, H. Zhu, Prediction and optimization of dimensional accuracy of inclined structures fabricated by laser powder bed fusion, *Journal of Manufacturing Processes* 81 (2022) 281–289.
- [45] Z. M. Taib, W. S. W. Harun, S. A. C. Ghani, M. Rashid, M. A. Omar, H. Ramli, Dimensional accuracy study of open cellular structure coCrMo alloy fabricated by selective laser melting process, *Advanced Materials Research* 1133 (2016) 280.